Resonance-Enhanced X-rays in Thin Films: A Structure Probe for Membranes and Surface Layers

Jin Wang, Michael J. Bedzyk, Martin Caffrey

An x-ray resonance effect in an organic thin film on an x-ray reflecting mirror is reported. The resonance effect is the result of interference between reflected and refracted x-rays at the air–organic thin film interface and occurs at incident angles slightly above the critical angle of the film. In excellent agreement with theory, the primary resonant x-ray electric field that is confined in the organic thin film is ~20 times as intense as the electric field of the incident beam when measured at a position close to the center of the film. Resonance-enhanced x-rays can be used to characterize the internal structure of Langmuir-Blodgett thin film membranes. This effect may also find use in x-ray–based thin film devices and in the structural analysis of adlayers and surfaces that have thus far proved difficult, if not impossible, to study because of sensitivity limitations.

Several important phenomena, such as total external reflection and the formation of evanescent and standing waves, are a consequence of the interaction of x-rays with flat surfaces or mirrors at glancing angles (*1–11*). These effects have found wide application in the characterization of surfaces and thin films. Recently, we have shown that an x-ray standing wave (XSW) generated during total external reflection at a gold mirror surface is well defined at ~1000 Å above the surface and that the useful probing distance of this element-specific XSW is also of this length scale (*10*). Calculations presented by Wang *et al.* [figure 3a of (*10*)] and in studies of de Boer (*11*) indicated the existence of a potentially useful resonance effect that markedly enhances the electric field (*E* field) of the penetrated x-rays in the organic thin film at low angles of incidence. Here, we demonstrate experimentally that the resonance effect is, in fact, real and explain its origin. Resonance-enhanced x-rays (REX) may find application in thin film and surface structure characterization.

X-rays undergo "total" external reflection from a flat surface at small subcritical angles of incidence. The critical angle, θ_c, for any x-ray mirror is defined as $\theta_c = (2\delta)^{1/2}$, where the refractive index of the mirror material is $n = 1 - \delta - i\beta$ (δ and β refer, respectively, to the x-ray scattering and absorption terms). In the vicinity of θ_c, the so-called evanescent wave effect (*3–6*) and refraction cause the *E* field intensity (*I*) at and immediately below the mirror surface to be larger than that of the incident beam, I_0 (Fig. 1).

J. Wang and M. Caffrey, Department of Chemistry and Chemical Physics Program, Ohio State University, Columbus, OH 43210.
M. J. Bedzyk, Department of Materials Science and Engineering, Northwestern University, Evanston, IL 60208, and Argonne National Laboratory, Argonne, IL 60439.

Resonance-enhanced x-rays are generated between two parallel x-ray–reflecting surfaces when they are separated by a medium that is suitably thick and x-ray–transparent and when they are illuminated by an incident x-ray plane wave with an extended footprint at an appropriate angle. Throughout the following discussion we assume that the x-ray beams remain coherent in and above the x-ray mirrors (*10*). For purposes of comparison with the experimental system used to demonstrate the existence of REX, the reader is referred to the model shown in Fig. 2A. It consists of two interfaces and three media, air, an organic thin film (925 Å thick), and a gold x-ray mirror, denoted by indices 1, 2 and 3, respectively. For incident x-rays at 9.8 keV, the corresponding δ values are as follows: δ_1 (0) < δ_2 (2.50×10^{-6}) < δ_3 (3.08×10^{-5}). In the figure the x-ray beams are labeled according to the notation of Born and Wolf (*12*) and are defined more fully in (*13*). When an x-ray beam, A_{12}, strikes the air-film (1 → 2) interface at an incident angle θ_1, slightly above the critical angle of the first interface (θ_{c1}, 2.236 mrad), it penetrates medium 2 at an angle θ_2, where $\theta_2 \approx (\theta_1^2 - \theta_{c1}^2)^{1/2}$ as a result of refraction at the interface. Because $\theta_2 << \theta_{2c}$ (the critical angle of the 2 → 3 interface, 7.523 mrad), the x-ray beam in medium 2 undergoes total external reflection at the 2 → 3 interface. Interference between the coherently related incident (A_{23}) and reflected (R_{23}) beams at and above the gold surface gives rise to an XSW as described previously (*7, 10*). The periodicity, *D*, of the XSW is related to θ_2 and to the x-ray wavelength, λ, as follows: $D = \lambda/(2 \sin\theta_2)$.

As θ_2 approaches 0.659 mrad (θ_1 = 2.331 mrad), the first antinode (maximum) of the XSW collapses inward toward the mirror surface and is positioned close to the center of the organic film. Concurrently, the first and second nodes (minima) of the XSW are located just below the 2 → 3 and exactly at the 1 → 2 interface, respectively (Fig. 2B, curve I, referred to as the first-order resonance condition). At the same time, the transmitted (T_{12}) and reflected (R_{21}) beams are in phase and interfere constructively. Furthermore, unlike the second interface in the Fabry-Perot interferometer (*12*), the 2 → 3 interface behaves as a perfect x-ray–reflecting mirror at these low angles of incidence. Thus, the x-rays entering the organic film become trapped and are bounced back and forth between the two interfaces, reducing the intensity of the reflection in medium 1. At resonance, the XSW *E* field in medium 2 within the footprint of the x-ray beam is greatly enhanced as a consequence of (i) constructive interference of T_{12} and R_{21} below the 1 → 2 interface, and (ii) the refraction-related enhanced transmitted *E* field of amplitude $T_{12} = A_{12}t_{12}$, where $|t_{12}| > 1$ at low incident angles and where the *E* field is intensified by the factor t_{12} (*13*).

Assuming ideal plane waves, we can use arguments similar to those described in (*12*) for multiple-beam fringes in a plane parallel

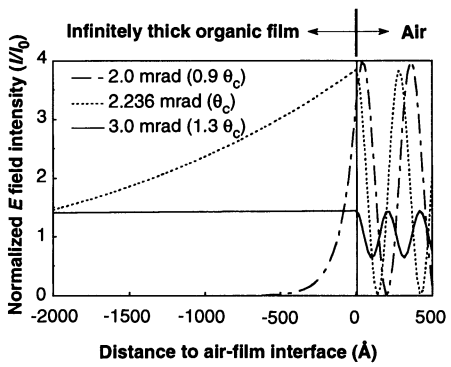

Fig. 1. The height dependence of the normalized *E* field intensity generated during specular reflection of a 9.8-keV x-ray plane wave from the surface of an infinitely thick organic film at different angles of incidence. The refractive index of the organic film is $1 - (2.5 \times 10^{-6}) - (2.24 \times 10^{-9})i$, and the critical angle of the air-film interface is 2.236 mrad. The damping *E* field below the mirror surface follows the absorption relation $I(\theta, z) = I_0\, T(\theta) \exp(-\mu_e z)$, where $T(\theta)$ is the surface intensity, μ_e is the effective linear absorption coefficient, and *z* is the distance below the surface in the organic film. At $\theta = 0.9\,\theta_c$ and θ_c, the *E* field intensity at the air-film interface is close to 4 I_0 as expected for surface enhancement. The markedly depressed *E* field intensity and the decrease in its modulation above θ_c arise because of low reflectivity in this angular range. The theoretical calculations presented in this figure and in Fig. 2B make use of Maxwell's equations and Fresnel coefficients. The corresponding theory is well established (*2–11, 17*).

plate system. In such a treatment, the amplitude of the E field just below the 1 → 2 interface in the transmission direction can be expressed as

$$E \approx A_{12}t_{12} \sum_{m=0}^{\infty} (\alpha^2 r_{21} r_{23})^m$$

$$= \frac{t_{12}}{1 - \alpha^2 r_{21} r_{23}} A_{12} \quad (1)$$

where t_{ij} and r_{ij} are the transmission and reflection coefficients at the $i \rightarrow j$ interface and α is the x-ray transmittance in medium 2. A more complete description of each of these terms is given in (*13*). Indeed, this resonance enhancement phenomenon occurs at incident angles where an XSW node coincides with the 1 → 2 interface [see (*14*) and Fig. 2B, curves II and III, referred to as second- and third-order resonant E field intensity profiles, respectively]. However, the magnitude of the resonance enhancement decreases with incident angle as a result of an abrupt drop in reflectivity at the 2 → 1 interface (r_{21}) and a diminished refraction-related enhancement effect (smaller t_{12}), while the reflectivity at the 2 → 3 interface (r_{23}) remains relatively constant until the critical angle, θ_{c2}, is reached.

The calculated E field intensity distribution in the organic thin film at different incident angles in the vicinity of θ_{c1} is presented in Fig. 2B. The resonance enhancement in the first-order peak (curve I) is immediately apparent and amounts to a factor of 43.4 times the E field intensity of the incident beam (with conventional XSWs the enhancement is fourfold). Resonance enhancement is dependent on, among other things, the thickness of the organic thin film. In the current model with an organic thin film having a refractive index of $1 - (2.5 \times 10^{-6}) - (2.24 \times 10^{-9})i$, resonance can be observed when the film thickness lies between 200 and 20,000 Å (data not shown). These limiting values are dictated, respectively, by the high and low angles of incidence necessary to satisfy the corresponding resonance conditions (*15*). By suitably adjusting the number and electron density of strata constituting medium 2, the fold enhancement of the E field at resonance can be increased significantly beyond the value of 43.4 as a result of interference and refraction-related enhancement at the multiple interfaces.

To verify experimentally the existence of REX in a mirror-supported thin film, we used the following strategy (see the inset in Fig. 3A): A hydrophobic gold mirror with 16 bilayers of ω-tricosenoic acid (ω-TA) and an inverted bilayer of zinc arachidate placed at the center of the lipid multilayer

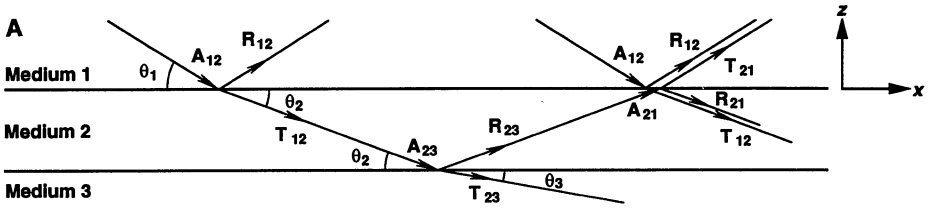

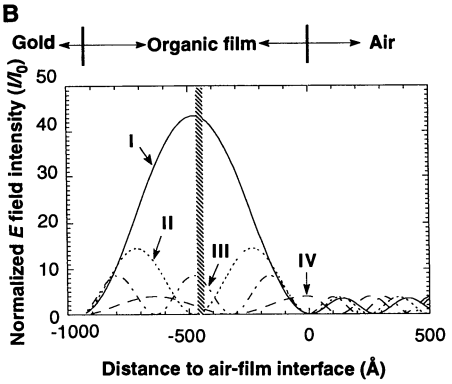

Fig. 2. Illustration of the calculated resonance-enhanced x-ray E field in a thin film and associated ray tracing diagram. (**A**) Schematic of the system under investigation (not drawn to scale) along with the relative positions of the incident (A), refracted or transmitted (T), and reflected (R) x-ray beams at the two interfaces formed by three stratified media as discussed in the text. On the right side of the diagram, the points of the intersection of rays A_{12} and A_{21} with the 1 → 2 interface have been displaced along the interface for purposes of clarity. (**B**) Height dependence of the normalized resonance-enhanced x-ray E field intensity generated by the interference of 9.8-keV x-ray plane waves reflected and refracted at two interfaces in an organic thin film on a gold mirror surface in air. The calculations are based on the following assumptions: organic film thickness = 925 Å; refractive indices of air, organic film, and gold are 1, $1 - (2.5 \times 10^{-6}) - (2.24 \times 10^{-9})i$, and $1 - (3.08 \times 10^{-5}) - (2.27 \times 10^{-6})i$, respectively, at 9.8 keV. Profiles I, II, and III represent the first-order (θ_1 = 2.331 mrad), second-order (θ_1 = 2.594 mrad), and third-order (θ_1 = 2.996 mrad) REX E field intensity distributions, respectively. The corresponding E field intensity maxima are 43.4, 14.5, and 8.5 I_0, respectively. Profile IV represents the E field intensity distribution at the off-resonance condition (θ_1 = 2.450 mrad), where peak intensity is 4 I_0 as is observed in a conventional XSW field. Separate calculations show that a relatively dilute heavy atom marker layer positioned in the organic overlayer (shaded rectangle) has a negligible effect on the E field intensity distribution in the film.

was prepared by the Langmuir-Blodgett (LB) technique. This arrangement places the heavy atom layer approximately at the center of the organic thin film. The photoelectric effect, evidenced by x-ray fluorescence, is proportional to the E field intensity at the center of the heavy atom probe layer by the dipole approximation. Thus, the intensity of probe x-ray fluorescence as a function of θ_1 in the vicinity of θ_{c1} is a direct measure of the E field intensity at the probe position in the adlayer. Placing the telltale heavy atom layer at the center of the organic thin film serves to sample the E field at its intensity maximum and minimum for the odd and even orders of resonance, respectively (see Fig. 2B) and, as a result, should reveal a similarly modulated fluorescence yield profile. The results of the x-ray fluorescence measurements made at the Cornell High Energy Synchrotron Source (CHESS) with an incident x-ray energy of 9.8 keV to optimally excite zinc fluorescence are presented in Fig. 3A. Exactly as predicted by theory, the data show the presence of an extremely large x-ray fluorescence peak slightly above the critical angle of the organic thin film.

The reflectivity data are shown in Fig. 3B. The presence of troughs in the reflectivity curve, which roughly align with the peaks and troughs in the corresponding fluorescence yield profile [(*16*), Fig. 3A], indicates that the reflected (R_{12}) and refracted (T_{21}) beams in air above the air-film interface are completely out of phase and interfere destructively at the resonance condition (Fig. 2A). The x-ray energy is in turn redistributed, and most of the energy is concentrated in the vicinity of the resonance peaks (antinodes) in the thin film at resonance. The direction of energy flow is parallel to the confining interfaces of the thin film. This result suggests an application for REX in x-ray–based microprobe devices.

The resonance effect described above arises as a result of a change in x-ray momentum transfer perpendicular to the interfaces, q_{z2} [$\approx (2 \sin\theta_2)/\lambda$], in the thin film. The experiments presented thus far involve adjusting q_{z2} by varying incident angle. We carried out a complementary measurement of the resonance effect brought about by adjusting wavelength, in the form of an energy scan. Because θ_{c1} changes with x-ray energy, an energy scan in the appropriate range on a sample held at a fixed angle will, at some point, bring θ_1 and θ_{c1} into close proximity. Thus, tuning the incident photon energy advances the XSW in the film, which, in turn, satisfies the resonant interference conditions described above (*14*). Such a measurement is presented in Fig. 4, which shows the energy-dependent zinc fluorescence at a fixed

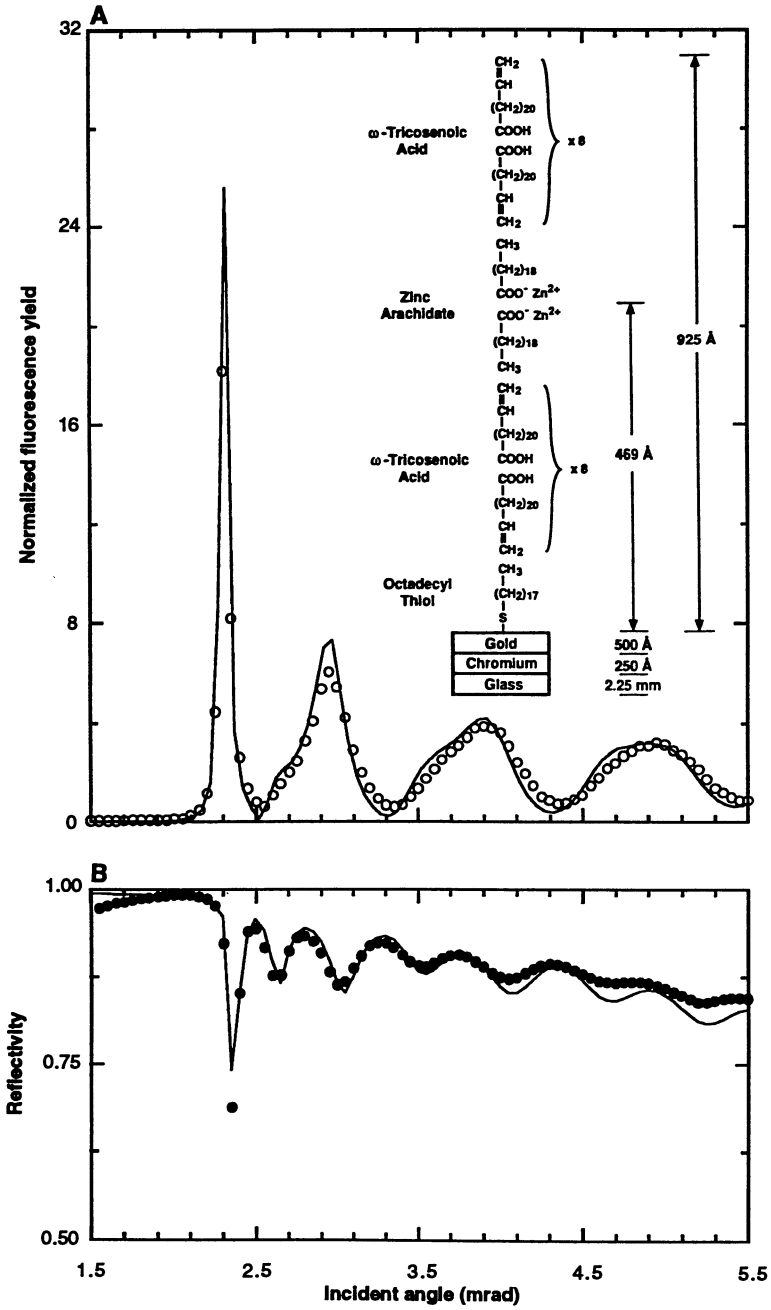

Fig. 3. Experimental (circles) and theoretical (——) angular dependence of (**A**) the zinc K_α fluorescence yield and (**B**) the specular reflectivity from the gold-supported LB multilayer samples at 9.8 keV. The fluorescence yield was normalized to the same area of illuminated film at all angles and scaled so that a fluorescence yield of unity was obtained far beyond the critical angle of the gold mirror. The reflectivity profile has twice as many modulations as the fluorescence yield profile because the zinc marker layer samples only the odd order *E* field peaks as shown in Fig. 2B. Fluorescence and reflectivity were measured with a monochromatic x-ray beam (19 μm high and 2.9 mm wide) obtained from a pair of silicon (111) crystals on the D-line at CHESS with the storage ring operating at 5.3 GeV and 65 to 85 mA total positron current. The experimental setup and data processing have been described (*7–10*). (Inset) Schematic of sample structure. The total and partial film thicknesses are indicated. In addition to the data reported above which focuses on the θ_{c1} region, more extensive x-ray fluorescence and reflectivity data were collected in the range 0 to 15 mrad. The reflectivity data were used to determine accurately lipid adlayer thickness at 925 Å while the fluorescence data provided details on the position of the heavy atom layer above the mirror surface (*7, 10*). These data show that the zinc layer is located at 468.5 Å above the surface with a spread (full width at half height) about the mean position of 14 Å. These values were used in calculating the theoretical curves shown in this figure (*18*).

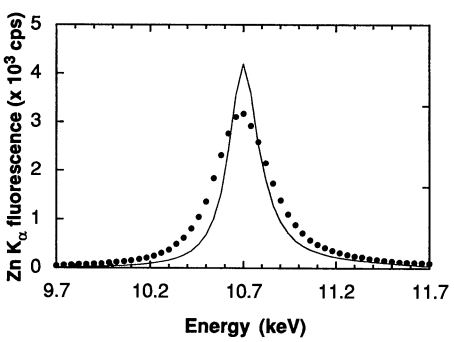

Fig. 4. First-order REX in the zinc-containing LB multilayer on a gold mirror monitored by measuring the x-ray energy dependence of the zinc K_α fluorescence at different incident angles. We collected the fluorescence data (●) using a counting time of 5 to 7 s per point and a dwell time of 1 s between points to allow the optical elements to stabilize after repositioning. Data have been corrected to a constant incident x-ray flux and constant absorption cross section over the entire energy range. The theoretical curve (——) is based on the assumption that the x-ray beam is monochromatic and collimated and that the sample interfaces are uniform and roughness-free. The resonance peak position in energy is extremely sensitive to incident angle. Because the incident x-ray beam has a finite, intrinsic divergence and because the sample surface is not perfectly uniform, it is expected that the observed experimental peak will be broader than the theoretical peak. The lower energy limit in the energy scan is set by the zinc K-absorption edge at 9.6 keV; background gold L-fluorescence (from the gold film, Fig. 2) above 11.9 keV dictates the upper limit.

angle of incidence. Once again, the enhanced resonance effect is apparent with maximum fluorescence at 10.7 keV (λ = 1.159 Å) as expected (Fig. 4).

The sizable intensity enhancement afforded by REX means that the significance of the effect goes beyond the realm of x-ray physics and devices such as x-ray microprobes and extends into the domain of thin film characterization. The pronounced sensitivity of the REX effect to film thickness can be taken advantage of in thin film characterization. REX should also find application in the characterization of surface films using extended x-ray absorption fine structure methods. With REX as the photon source, such measurements can be carried out on more dilute systems and with low–atomic number elements. Combined with state-of-the-art thin film preparation techniques, it should be possible to fabricate REX-based x-ray thin film devices such as x-ray microprobes, resonance cavities, and wave guides.

As part of a research program concerned with membrane protein structure, we use XSWs to investigate the topology of membrane proteins. One limitation in this application is sensitivity because heavy atom surface density can be quite low (10^{10} to 10^{12} atoms/cm^2) when each protein is tagged with just a single heavy atom. This resonance effect, which intensifies the probing *E* field in the region of interest, will compensate for the limiting surface density. Thus, important membrane, surface, and interfacial problems that cannot be analyzed with current methods because of low sensitivity may now become tractable as a result of exploitation of the resonance ef-

fect. A particularly promising application for REX in this context concerns the study of light-driven (and other stimulus-driven) processes such as transduction in the membrane-associated visual pigment protein, rhodopsin.

REFERENCES AND NOTES

1. A. H. Compton and S. K. Allison, *X-Rays in Theory and Experiment* (Van Nostrand, New York, 1935).
2. L. G. Parratt, *Phys. Rev.* **95**, 359 (1954).
3. W. C. Marra, P. M. Eisenberger, A. Y. Cho, *J. Appl. Phys.* **50**, 6927 (1979).
4. R. S. Becker, J. A. Golovchenko, J. R. Patel, *Phys. Rev. Lett.* **50**, 153 (1983).
5. J. M. Bloch *et al.*, *ibid.* **54**, 1039 (1985).
6. P. M. Eisenberger and W. C. Marra, *ibid.* **46**, 1081 (1981).
7. M. J. Bedzyk, G. M. Bommarito, J. S. Schildkraut, *ibid.* **62**, 1376 (1989).
8. M. J. Bedzyk, D. H. Bilderback, G. M. Bommarito, M. Caffrey, J. S. Schildkraut, *Science* **241**, 1788 (1988).
9. M. J. Bedzyk, G. M. Bommarito, M. Caffrey, T. L. Penner, *ibid.* **248**, 52 (1990).
10. J. Wang, M. J. Bedzyk, T. L. Penner, M. Caffrey, *Nature* **354**, 377 (1991).
11. D. K. G. de Boer, *Phys. Rev. B* **44**, 498 (1991).
12. M. Born and E. Wolf, *Principles of Optics* (Pergamon, Oxford, ed. 6, 1991).
13. Labeling of the various incident (A), refracted or transmitted (T), and reflected (R) beams in the current two-interface system is shown in Fig. 2A. The subscripts, *ij*, refer to the media *i* and *j*. Thus, R_{ij} corresponds to the beam reflected back into medium *i* upon striking the $i \rightarrow j$ interface; A, T, and R also correspond to the amplitudes of the respective *E* fields. With the exception of A_{12}, all *E* field amplitudes are functions of incident angle and obey Fresnel theory (*1, 2, 12*). The transmission and reflection coefficients are defined by $r_{ij} = R_{ij}/A_{ij}$ and $t_{ij} = T_{ij}/A_{ij}$, respectively. The x-ray transmittance in medium 2 defined by
$$\alpha = \frac{A_{23}}{T_{12}} = \frac{A_{21}}{R_{23}}$$
is a complex factor which accounts for the attenuation and phase change of the x-ray beam traversing the medium.
14. For a given XSW period and the interface phase shift as described in (*7*), *n*th order resonance is observed when the incident angle θ_2 satisfies approximately the following relation
$$d = \frac{\lambda}{2 \sin\theta_2}\left[n - \frac{1}{2} - \frac{1}{2\pi}\cos^{-1}\left(2\frac{\theta_2^2}{\theta_{c2}^2} - 1\right)\right]$$
where *d* is the thickness of medium 2.
15. According to (*14*), as medium 2 thins, the angle of incidence at which the resonance effect is observed increases. At the higher angles of incidence, however, the enhancement effect lessens because of a dramatic reduction in r_{21} and t_{12} (see Eq. 1). At the other extreme, where there is a thicker medium 2, the enhancement effect is less as a result of a reduction in transmittance, α, which is associated with a more profound attenuation of the x-ray beam in the thicker layer occurring at lower angles of incidence.
16. The term "roughly" is used to indicate that the alignment of troughs in the reflectivity curve with peaks and troughs in the fluorescence curve is not exact. The mismatch arises primarily because the probing heavy atom layer is placed slightly off the center position in medium 2.
17. G. M. Bommarito, thesis, Cornell University, Ithaca, NY (1987).
18. Because the thickness of the heavy atom probe layer is small (10 to 15 Å) compared to the width of the resonant *E* field intensity peak (~500 Å, Fig. 2B), the x-ray fluorescence is a reliable and a direct measure of the *E* field intensity at the position of the heavy atom probe layer in the adlayer with a spatial resolution of better than 20 Å. The mismatch in the height of the experimental and theoretical curves in Fig. 3A arises from nonuniformities in the organic thin film and from a finite divergence of the incident x-ray beam (~50 μrad full width at half maximum) not corrected for in the calculations.

19. This work was supported by grants from the National Institutes of Health (DK 36849 and DK 45295), a University Exploratory Research Program Award (Procter and Gamble Company), and a DuPont Young Faculty Award to M.C.; by separate grants from Eastman Kodak Company to M.J.B. and M.C.; and by a Grant-in-Aid of Research from Sigma Xi, the Scientific Research Society, to J.W. CHESS is supported by a grant from the National Science Foundation (DMR 90-21700).

21 April 1992; accepted 11 August 1992

Submicrometer Intracellular Chemical Optical Fiber Sensors

Weihong Tan, Zhong-You Shi, Steve Smith, Duane Birnbaum, Raoul Kopelman*

A thousandfold miniaturization of immobilized optical fiber sensors, a millionfold or more sample reduction, and at least a hundredfold shorter response time, all simultaneously, were achieved by combining nanofabricated optical fiber tips with near-field photopolymerization. Specifically, pH optical fiber sensors were prepared with internal calibration, making use of the differences in both fluorescence and absorption of the acidic and basic dye species. The submicrometer sensors have excellent detection limits, as well as photostability, reversibility, and millisecond response times. Successful applications include intracellular and intraembryonic measurements. Potential applications include spatially and temporally resolved chemical analysis and kinetics inside single biological cells and their substructures.

Chemical concentration gradients and spatial heterogeneities are of great interest in many areas, including analytical chemistry, cell biology, physiology, toxicology, and materials science. In cell biology, for example, intracellular measurements could produce concentration profiles of cytoplasms. Probes of very small size are needed to make such measurements. In this report, we describe a technology that enables the development of optical fiber sensors with submicrometer to tens of micrometer dimensions and extremely short response times. These sensors serve as nonperturbative probes for the measurement of microscopic and submicroscopic chemical profiles and their time development.

Electrically based sensors with submicrometer dimensions and subsecond response times have been used to probe chemical concentrations that are spatially heterogeneous (*1*). However, this is not the case for optical fiber sensors, which have been widely used in recent years (*2–4*) and have demonstrated several advantages over electrically based sensors (*2–3*). The most important disadvantage has been the absence of an optical fiber sensor small enough to probe spatial, chemical, or biological heterogeneities in the submicrometer size range. The smallest optical fiber sensor reported to date is about 100 μm, requires a sample volume of microliters, and has a response time of several seconds. We have developed an optical fiber sensor for spatially heterogeneous measurements, with sizes as small as 0.1 μm and sample volume requirements on the order of femtoliters. At the same time, these new optical fiber sensors are also capable of fast (millisecond) monitoring of chemical and biological reactions, for example, chemical kinetics inside restricted intracellular domains, where nonclassical rate laws apply (*5*).

There are two major difficulties in making small-sized optical fiber sensors. One is the limitation in most of the available techniques for the attachment of chemicals or biological reagents to the fiber surface. The attachment of chemical or biological reagents by membranes or tubing or any other mechanical method makes only very limited use of the fiber tip surface, which results in very weak signals and very slow response times. The covalent immobilization of reagents by photopolymerization on the distal end of an activated fiber has solved this problem (*3, 4*). In this approach, the polymer serves to increase the surface area, which results in multiple reagent immobilization sites. Because there is no need for the use of a membrane or other mechanical means of confinement, the response is faster and the manufacturing is easier. The second difficulty in fabricating small optical fiber sensors is that there are no optical fibers of sufficiently small size commercially available. The smallest optical fiber sold commercially is still in the

Department of Chemistry, University of Michigan, Ann Arbor, MI 48109.

*To whom correspondence should be addressed.